

Coherent pathways for subduction from the surface mixed layer at ocean fronts

Mara Freilich¹, Amala Mahadevan²

¹MIT-WHOI Joint Program in Oceanography/Applied Ocean Sciences and Engineering

²Woods Hole Oceanographic Institution

Key Points:

- The dynamical pathways of subduction from the surface mixed layer to the pycnocline at a front are characterized using Lagrangian analysis.
- The pathways of subduction are influenced by mixed layer mesoscale (geostrophic) and submesoscale (ageostrophic) frontogenetic processes.
- Due to the influence of submesoscale along-front variability, subduction is coherent on submesoscale, ~ 10 km, length scales.

Corresponding author: Mara Freilich, maraf@mit.edu

Abstract

In frontal zones, water masses that are tens of kilometers in extent with origins in the mixed layer can be identified in the pycnocline for days to months. Here, we explore the pathways and mechanisms of subduction, the process by which water from the surface mixed layer makes its way into the pycnocline, using a submesoscale-resolving numerical model of a mesoscale front. By identifying Lagrangian trajectories of water parcels that exit the mixed layer, we study the evolution of dynamical properties on subducting water parcels from a statistical standpoint. Velocity and buoyancy gradients increase as water parcels experience both mesoscale (geostrophic) and submesoscale (ageostrophic) frontogenesis and subduct beneath the mixed layer into the stratified pycnocline along isopycnals that outcrop in the mixed layer. Subduction is transient and occurs in coherent regions along the front, the spatial and temporal scales of which set the scales of the subducted water masses in the pycnocline. As a result, the tracer-derived vertical transport rate spectrum is flatter than the vertical velocity spectrum. An examination of specific subduction events reveals a range of submesoscale features that support subduction. Contrary to the forced submesoscale processes that sequester low potential vorticity (PV) anomalies in the interior, we find that PV can be elevated in subducting water masses. The rate of subduction is of similar magnitude to previous studies (~ 100 m/year), but the pathways that are unraveled in this study along with the Lagrangian evolution of properties on water parcels, emphasize the role of submesoscale dynamics coupled with mesoscale frontogenesis.

Plain Language Summary

Exchange of properties such as heat, carbon, and nutrients between the ocean surface and the interior has implications for ocean circulation and ecosystems. But the sharp increase in density below the well-mixed surface layer, inhibits the transport of these waters into the region of increasing density that lies beneath, except along sloping surfaces of constant density or fronts. Here, we use a computational ocean model of an ocean front, to track the water that exits the surface layer to travel deeper and study its properties. The vertical movement occurs in specific regions, at scales $\lesssim 10$ km, as the horizontal density variation increases. The rate of subduction due to these small-scale processes is the same magnitude as the rate of subduction reported in previous studies that only included larger-scale mesoscale processes, representing important pathways for exchange between the surface and interior that are not included in global models and are difficult to observe.

1 Introduction

The exchange of properties between the ocean and atmosphere, including heat, carbon, and oxygen, is affected by the transport of water from the surface mixed layer into the stratified pycnocline. This transport across the strongly stratified base of the mixed layer ventilates the pycnocline, affects the water mass characteristics of the interior, and has a large impact on the ocean’s biogeochemistry. The process of *subduction*, defined here as the transport of water from the mixed layer into the stratified pycnocline, has been studied at the basin scale via the seasonal transformation of the mixed layer and the large-scale circulation (Nurser & Marshall, 1991). There is now increasing recognition of the role that submesoscale processes play in this exchange by generating large vertical velocities over short spatial and temporal scales (Bosse et al., 2015; Omand et al., 2015; Klymak et al., 2016; Stanley et al., 2017; Wenegrat et al., 2018). Our objective is to study the dynamical processes and pathways through which the mixed layer and pycnocline connect, and to provide insight into the subduction mechanisms as well as the scales of transport.

Large vertical velocities in the mixed layer can arise from a range of submesoscale processes (Haine & Marshall, 1998; Mahadevan & Tandon, 2006; McWilliams, 2016). These include mixed layer instability (Fox-Kemper et al., 2008), submesoscale frontogenesis in the mixed layer (Thomas et al., 2008; Barkan et al., 2019), and boundary forced submesoscale dynamics, such as non-linear Ekman pumping and surface-forced symmetric instability (Thomas et al., 2013), which generate vertical velocities of $\mathcal{O}(100)\text{m-d}^{-1}$ (Fox-Kemper et al., 2008; Mahadevan et al., 2010). Submesoscale flows are characterized by large, $O(1)$, Rossby number, and low (also, $O(1)$) Richardson number. The downward velocities due to submesoscale dynamics are larger in magnitude and concentrated in smaller regions than the upward velocities (Shcherbina et al., 2015). Boundary layer turbulent motion at mixed layer fronts, which is resolved by large eddy simulations (LES) (Skylvingstad et al., 2017; Verma et al., 2019) and observed with Lagrangian instruments (D’Asaro et al., 2018) have recorded vertical velocities of $\mathcal{O}(1000)\text{m-d}^{-1}$ within the mixed layer. However, the vertical density gradient (stratification) at the base of the mixed layer is typically much greater than in the pycnocline and vertical transport across the mixed layer base is limited, with submesoscale instabilities confined to the mixed layer. In fact, the parametrization of mixed layer instability (Fox-Kemper et al., 2008) describes the vertical buoyancy flux as maximal in the middle of the mixed layer, and diminishing toward mixed layer base, without accounting for exchange between the mixed layer and pycnocline.

However, submesoscale dynamics may also have an influence below the surface mixed layer. Symmetric instability mixes momentum and tracers along isopycnal surfaces, of-

ten reaching below the mixed layer (Thomas et al., 2013) and leading to exchange of tracers between the surface and pycnocline (Smith et al., 2016; Erickson & Thompson, 2018; Archer et al., 2020). Submesoscale mixed layer eddies can also barotropize and induce along-isopycnal stirring in the pycnocline (Badin et al., 2011). Furthermore, recent observational and modeling studies have shown that large vertical buoyancy fluxes within the pycnocline have characteristic spatial and temporal scales of submesoscale processes (Yu et al., 2019; Siegelman et al., 2020) that may be attributable to geostrophic frontogenesis (Siegelman, 2020). These studies raise the possibility that surface-enhanced submesoscale dynamics may influence the pycnocline directly through water mass exchange.

The implications of vertical motion for water masses and biogeochemistry depend on the spatial and temporal scales of the transport. For water mass formation and carbon sequestration on annual time scales, subduction below the wintertime mixed layer is important and involves the seasonal evolution of the mixed layer (Lévy et al., 2013). However, subduction on sub-seasonal timescales is also relevant for the mesopelagic supply of organic carbon and oxygen, which impacts ecological processes below the mixed layer.

Besides mixing, there are two main processes that could diabatically subduct water parcels from the mixed layer. The first is restratification of the mixed layer. As the mixed layer restratifies due to either heat fluxes or the slumping of isopycnals (Fox-Kemper et al., 2008; Mahadevan et al., 2012), some water parcels end up beneath the newly reformed mixed layer. The second process, which will be the focus of this paper, involves movement along sloping density surfaces. If a density surface from the pycnocline outcrops into the mixed layer, then water parcels can move adiabatically along that surface from the mixed layer into the interior. This process has been described on the basin scale (Stommel, 1979; Nurser & Marshall, 1991) and mesoscale (Gebbie, 2007; MacGilchrist et al., 2017) and may be important on the submesoscale as well (Canuto et al., 2018).

Frontal regions, where sloping isopycnals from the pycnocline outcrop in the surface mixed layer, offer an advective pathway for the exchange of water across the base of the mixed layer (Ramachandran et al., 2014). Frontogenesis, which is the intensification of lateral buoyancy (or density) gradients at fronts, dynamically induces subduction (and upwelling) along the sloping isopycnal surfaces of the front and does not necessarily involve the shoaling of the mixed layer. It could contribute significantly to the exchange of biogeochemical properties and water masses. Submesoscale instabilities can occur along strong mesoscale currents (Thomas & Joyce, 2010; Gula et al., 2016), enhancing vertical motion and generating an asymmetry in the up-/down-ward motion, with subduction being more localized and intensified than upwelling.

Water masses that are subducted from the surface mixed layer into the pycnocline can have anomalously low stratification and potential vorticity (PV) compared to surrounding waters and develop anticyclonic relative vorticity (Pollard & Regier, 1992). However, subduction of biogeochemical tracers can occur along sloping density surfaces even without generating a volume anomaly and therefore could also occur along high PV pathways (Freilich & Mahadevan, 2019).

In this study, we focus on the dynamical aspects of subduction at ocean fronts, when the mixed layer is not undergoing restratification. We use numerical modeling to interrogate the coupling between mesoscale and submesoscale processes along a strong mesoscale frontal meander with a 50–70 m deep mixed layer. The model is representative of the front between Atlantic and Mediterranean waters in the Alborán Sea, where the subduction of biogeochemical tracers was observed along a mesoscale frontal meander (Pascual et al., 2017; Ruiz et al., 2019). We do not force the model with winds or strong buoyancy fluxes at the surface, which would generate boundary layer turbulence with large vertical velocities in the mixed layer. Further, we do not resolve processes at scales smaller than 500 m, such as symmetric instability. Instead, we follow the evolution of dynamical and kinematic properties as water subducts out of the mixed layer. This occurs along isopycnal surfaces along the front. Our objective is to examine the mechanism of subduction via frontogenesis, while also identifying where, when, and on what spatial (and temporal) scales subduction occurs. We also identify the physical features that carry water to depth and the characteristics of the subducted water masses that may help to identify them in observations.

We carry out a Lagrangian analysis of subduction to describe the mechanisms for transport of mixed layer water masses into the pycnocline. Studying frontogenesis in the Lagrangian frame overcomes some limitations of the Eulerian frame. Firstly, the time history of processes on a water parcel as they evolve over a few days provides information about subduction. We are interested in transport, and not vertical velocity by itself. Transport is integrated motion over a few days, while the vertical velocity field also contains waves and other high frequency motions. Secondly, while we are interested in the downward motion of water, the along-front flow is faster by 3–4 orders of magnitude. Hence, snapshot views of frontal cross-sections do not convey where the subducting water originates, or where it is headed. Thirdly, subduction does not occur everywhere along the front and to identify where it occurs, and on what spatial scales, we need to tag the water parcels that subduct. Following the advecting water parcels as they subduct allows us to construct a time history of the mechanisms. We define subduction as occurring when water parcels leave the mixed layer and travel at least 5 m below the mixed layer base into the pycnocline. By identifying the locations where water leaves the mixed

layer, we examine the spatial scales of the process. The evolution of dynamical properties along water parcel trajectories reveals how frontogenesis acts to subduct water, but that there are a wide variety of subduction pathways along which the dominant frontogenetic and frontolytic factors can differ (Thomas, 2008; Barkan et al., 2019).

To begin, we discuss observations of subduction at the front between fresher (less dense) Atlantic water and saltier (denser) Mediterranean water from the Alboran Sea. Next, we offer some theoretical background based on which we develop hypotheses about the subduction processes. We then describe our idealized model and the Lagrangian methodology used for analysis. In our results, we present a statistical view, as well as a description of specific subduction pathways. Finally, we offer a discussion of our results and their implications in a broader context.

2 Observational motivation

In March and April of 2019 we embarked on an observational campaign to study the pathways of vertical transport of natural tracers from the surface ocean to the interior. We conducted hydrographic surveys on board the *N/O Pourquoi Pas?* from March 28–April 11 at strong mesoscale and submesoscale fronts in the Alborán Sea (Western Mediterranean) (Mahadevan et al., 2020). These observations are used to motivate this study and provide observational context for the modeling results. We measured conductivity, temperature, and pressure using an *Oceansciences* underway CTD system while the ship was transiting across fronts (Johnston et al., 2019). Profiles are at a spatial resolution of around 1 km from the underway CTD operated in tow-yo mode. The velocities measurements are from a 150 kHz vessel-mounted ADCP.

The Western Alborán Gyre is formed by the mesoscale meander of the baroclinically unstable front between the saltier resident Mediterranean water and the fresher Atlantic water that enters through the strait of Gibraltar (Figure 1A; longitudes 3.5W to 5.5W). We traversed across the front several times, and Figure 1B shows, as an example, the hydrography from a section across the northern edge of the Western Alborán Gyre. The density gradient at the front is mostly due to salinity. Variations in temperature along a density surface are indicative of subduction or stirring of water masses. There are multiple warm intrusions that extend from the surface into the pycnocline along isopycnals. Though these intrusions are visible in the cross-front direction, they are also expected to be moving rapidly in the along-front direction (out of the page in Figure 1B). Casts from a shipboard CTD show that these temperature anomalies are associated with unusually high fluorescence and low apparent oxygen utilization for the depth at which they occur, adding support to the idea that these are recently subducted water masses. The along-track vorticity, which, despite neglecting cross-track gradients, is a good es-

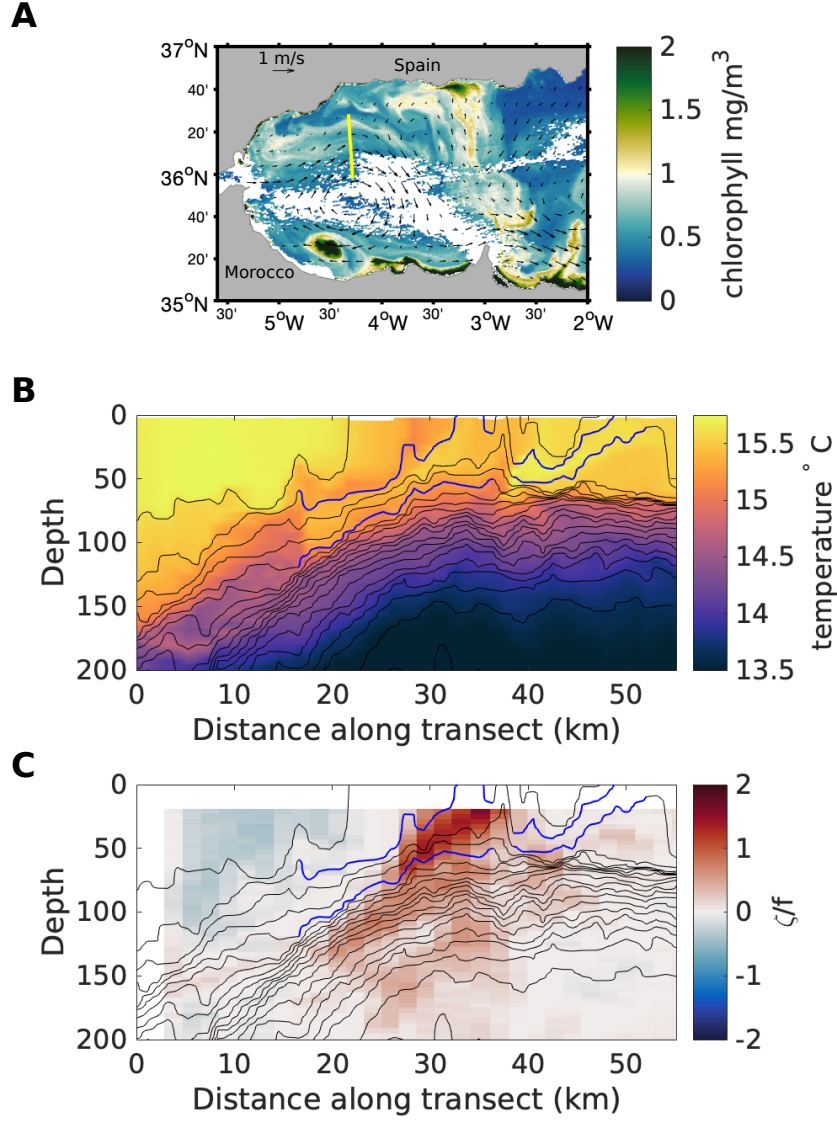


Figure 1. (a) MODIS Aqua satellite image of chlorophyll in the Alborán Sea on March 28, 2019. The geostrophic currents from AVISO (arrows) show the anticyclonic Western Alborán Gyre. The chlorophyll (in color) shows the influence of frontal dynamics at the gyre edge with with frontal waves on the northern edge of the gyre. The CALYPSO cruise on the *N/O Pourquoi Pas?* surveyed the front along the yellow line on March 30, 2019. (b) Transect of temperature (color) from an underway CTD with density contours at intervals of 0.1 kg/m^3 . Subducted water masses are identified by temperature variations along an isopycnal surface. (c) Transect of relative vorticity computed approximately as the along-track gradient of the velocity normal to the ship is based on velocity measurements from a vessel-mounted ADCP. Two warm intrusions that are notable from the temperature section are highlighted with blue lines along isopycnal and are indicative of subduction. The ship transited from south to north.

194 timate of the relative vertical vorticity, because the ship traverses across the front has
 195 large ($\approx 2f$), surface-intensified cyclonic values at the center of the front (Figure 1C).
 196 On the dense side of the front, the vorticity is weakly cyclonic while on the light side of
 197 the front the vorticity is weakly anticyclonic. The cyclonic vorticity reaches $2f$ at the
 198 center of the front.

199 The surface chlorophyll image shows high chlorophyll on the gyre edge that forms
 200 frontal waves or cusp-like features (Figure 1A), one of which is sampled by the ship tran-
 201 sect. The feature on the northern flank of the front is found to be an eddy, 10 km in di-
 202 ameter and 70 m deep (Figure 1B). There is a temperature intrusion wrapped around
 203 the submesoscale eddy on the dense side of the front, which extends from the surface to
 204 the upper pycnocline (Figure 1B). Despite the light core, this eddy has cyclonic vortic-
 205 ity (Figure 1C); the cusps in the chlorophyll image also suggest cyclonic rotation. A sim-
 206 ilar feature is found in the modeling study that follows. Another temperature intrusion
 207 is co-located with the high relative vorticity at the center of the front, where density sur-
 208 faces from the upper pycnocline outcrop (Figure 1B,C). The intrusion extends 100 m in
 209 the vertical and 30 km in the north-south direction along density surfaces. On the deep
 210 end of this temperature intrusion, the feature has anticyclonic vorticity and reduced strat-
 211 ification.

212 These observations reveal pathways of natural tracers from the surface mixed layer
 213 to the upper pycnocline that are coherent over scales of tens of kilometers. The verti-
 214 cal transport associated with these features is on the order of 100 meters. Contrary to
 215 some previous observations (e.g. (Archer et al., 2020)), these subducted features are as-
 216 sociated with strong cyclonic vorticity, rather than anticyclonic vorticity. Some past ob-
 217 servations have also observed temperature-salinity intrusions within the pycnocline that
 218 do not present as low PV anomalies (Beaird et al., 2016). We use a process study model
 219 to examine the role that unforced frontal dynamics might have played in these observed
 220 subduction events, elaborate on the dynamical mechanisms of subduction, and describe
 221 the role of along-front variability in subduction from the surface mixed layer to the in-
 222 terior.

223 3 Theoretical background

The lateral buoyancy (and density) gradient at ocean fronts can be intensified through
 the mechanism of frontogenesis. Here, buoyancy $b \equiv -\frac{g}{\rho_0}(\rho - \rho_0)$, where ρ is the po-
 tential density, $\rho_0 = 1027 \text{ kg m}^{-3}$ is a reference potential density, and g is the accel-
 eration due to gravity. The vertical and horizontal buoyancy gradients are denoted by
 $N^2 = b_z$ and $M^2 = |\nabla_h b|$. Treating buoyancy as a conserved tracer, i.e. $Db/Dt = 0$,
 where D/Dt is the material derivative, the Lagrangian rate of change of buoyancy gra-

dients in the horizontal plane can be expressed as

$$\frac{D}{Dt} \nabla_h b = \underbrace{(-u_x b_x - v_x b_y, -u_y b_x - v_y b_y)}_{\mathbf{Q}} - N^2 \nabla_h w + \kappa \nabla_h^2 \nabla_h b + \nu \frac{\partial^2}{\partial z^2} \nabla_h b, \quad (1)$$

where ∇_h is the horizontal gradient operator in the x - y plane. Here, κ , the horizontal diffusivity and ν , the vertical diffusivity are treated as homogeneous and constant. The vector \mathbf{Q} on the right hand side of (1), is the tendency of advection to strengthen or weaken buoyancy gradients in the x and y directions and can be decomposed into geostrophic and ageostrophic contributions $\mathbf{Q} = \mathbf{Q}_g + \mathbf{Q}_a$ by using the respective geostrophic or ageostrophic components of the horizontal velocity $\mathbf{u} = \mathbf{u}_g + \mathbf{u}_a$. The square of the magnitude of frontogenetic tendency (a scalar quantity) is given by

$$\frac{D}{Dt} |\nabla_h b|^2 = \underbrace{\mathbf{Q}_g \cdot \nabla_h b}_{\text{geostrophic}} + \underbrace{\mathbf{Q}_a \cdot \nabla_h b}_{\text{ageostrophic}} - \underbrace{N^2 \nabla_h w \cdot \nabla_h b}_{\text{vertical}} + \underbrace{\kappa \nabla_h^2 \nabla_h b \cdot \nabla_h b}_{k_h} + \underbrace{\nu \frac{\partial^2}{\partial z^2} \nabla_h b \cdot \nabla_h b}_{k_v}. \quad (2)$$

The large-scale straining that intensifies buoyancy gradients disrupts the thermal wind balance and generates ageostrophic circulation in the vertical plane (Hoskins & Bretherton, 1972).

The resulting vertical velocity, w , can be diagnosed from the observed frontogenetic strain (Hoskins et al., 1978) using the Omega equation, which has been applied in a wide range of oceanic and meteorological contexts. Combining the quasigeostrophic momentum and mass conservation equations gives the ageostrophic circulation

$$N^2 \nabla_h w - f_0 \frac{\partial \mathbf{u}_a}{\partial z} = 2\mathbf{Q}, \quad (3)$$

where N^2 is the vertical buoyancy gradient, f_0 is a reference Coriolis parameter, and \mathbf{u}_a is the ageostrophic horizontal velocity vector. The divergence of (3) gives the classical Omega equation

$$N^2 \nabla_h^2 w - f_0 \frac{\partial^2 w}{\partial z^2} = 2\nabla \cdot \mathbf{Q}. \quad (4)$$

For a more detailed derivation see Section 13.3 of (Hoskins & James, 2014). In the quasigeostrophic formulation of the Omega equation, $\mathbf{Q} = \mathbf{Q}_g$ contains only geostrophic velocities (\mathbf{u}_g), so the ageostrophic velocity and the vertical velocities are forced by only geostrophic straining. The lack of a feedback from ageostrophic velocities generated by frontogenesis implies that both cyclonic and anticyclonic vorticity increase at the same rate and that the intensity of the upward and downward vertical velocities is symmetric (Hoskins & Bretherton, 1972), both of which are not true at the oceanic submesoscale (Shcherbina et al., 2015).

The semigeostrophic Omega equation includes a feedback between the ageostrophic velocity and the frontal intensity by allowing for advection of buoyancy and geostrophic

237 velocities by the combined geostrophic and ageostrophic velocities. To obtain the diag-
 238 nostic equation for the vertical velocity, the horizontal coordinates are transformed into
 239 geostrophic coordinates

$$X = x + v_g/f_0$$

$$Y = y - u_g/f_0.$$

The semigeostrophic Omega equation is then

$$\nabla_h^2 q_g w^* + f_0^2 \frac{\partial^2 w^*}{\partial z^2} = 2\nabla \cdot \mathbf{Q} \quad (5)$$

where $w = (1 + \zeta_g/f_0)w^*$ and ζ_g is the geostrophic relative vorticity. Here, N^2 on the left hand side of the quasigeostrophic Omega equation (3) is replaced by the quasigeostrophic PV in the transformed coordinates defined as

$$q_g = \left(1 + \frac{\zeta_g}{f_0}\right) N^2. \quad (6)$$

The derivatives in the \mathbf{Q} -vector in (5) are in geostrophic coordinates, such that

$$\mathbf{Q} = \left(-\frac{\partial u}{\partial X} \frac{\partial b}{\partial X} - \frac{\partial v}{\partial X} \frac{\partial b}{\partial Y}, -\frac{\partial u}{\partial Y} \frac{\partial b}{\partial X} - \frac{\partial v}{\partial Y} \frac{\partial b}{\partial Y} \right). \quad (7)$$

The ageostrophic circulation that results from mesoscale strain is frontogenetic (buoyancy gradient increasing) on the dense side of the front and frontolytic (buoyancy gradient decreasing) on the light side of the front (Hoskins & Bretherton, 1972). The resulting ageostrophic circulation is skewed with larger magnitude downward velocities and larger magnitude cyclonic vorticity (Hoskins, 1982). The non-linear feedback on the relative vorticity is evident from the Lagrangian rate of change of the absolute vorticity (ω_a) given by

$$\frac{D\omega_a}{Dt} = (\omega_a \cdot \nabla) \mathbf{u} + \frac{1}{\rho^2} \nabla \rho \times \nabla p + \nu \nabla^2 \omega_a. \quad (8)$$

Assuming adiabatic dynamics, the rate of change of the vertical component of the relative vorticity (ζ) is dominated by the vortex stretching and tilting terms on the rhs of the equation.

$$\frac{D(f + \zeta)}{Dt} = (f + \zeta) \frac{\partial w}{\partial z} + \frac{1}{\rho^2} \left(\frac{\partial \rho}{\partial x} \frac{\partial p}{\partial y} - \frac{\partial \rho}{\partial y} \frac{\partial p}{\partial x} \right). \quad (9)$$

240 At surface convergences (positive w_z), the near surface vertical velocity is downwards
 241 (negative) and the relative vorticity increases exponentially. However, at divergences (neg-
 242 ative w_z), the absolute vorticity ($f + \zeta$) decreases and approaches zero, which slows the
 243 rate of decrease of relative vorticity. In addition, if the vertical component of the abso-
 244 lute vorticity is negative, the system becomes symmetrically unstable. Symmetric insta-
 245 bility will restore the PV to zero, which limits the relative vorticity to $\zeta \geq -f$.

246 The ageostrophic circulation obtained from the semigeostrophic Omega equation
 247 is more along-isopycnal than the ageostrophic circulation obtained from the quasigeostrophic

Omega equation. The semigeostrophic Omega equation predicts that downward vertical velocity from the surface will be concentrated in a smaller area and therefore of larger magnitude than the upwelling vertical velocity. Moreover, the downward vertical velocity will be associated with large cyclonic vorticity. There are, however, additional processes that are not included in this equation. Diabatic processes including mixing are particularly important at the sharp fronts that are present at submesoscales and could be included in a generalized semigeostrophic omega equation (Giordani et al., 2006).

Another useful principle for examining subduction is the conservation of potential vorticity (PV). The PV and vertical velocity are related dynamically (Thomas et al., 2008). The Ertel PV is

$$q = \omega_a \cdot \nabla b = \underbrace{(w_y - v_z)b_x + (u_z - w_x)b_y}_{q_h} + \underbrace{(f + v_x - u_y)b_z}_{q_v}, \quad (10)$$

where q_v and q_h are the vertical (vortical) and horizontal (baroclinic) contributions to the PV, respectively. PV is conserved along a water parcel trajectory in the absence of diabatic processes. The PV is often simplified to just the vertical component of the PV, such that

$$\frac{Dq_v}{Dt} = N^2 \frac{D(f + \zeta)}{Dt} + (f + \zeta) \frac{DN^2}{Dt} = 0, \quad (11)$$

where $\zeta \equiv v_x - u_y$ is the vertical component of the relative vorticity and $N^2 \equiv b_z$. By examining (11), we can see that as a water parcel moves from the surface mixed layer and into the stratified interior such that the stratification (N^2) on the water parcel increases (“vortex squashing”), the relative vorticity on the water parcel must decrease. According to (9), $w_z < 0$ such that the vertical velocity decreases as the water parcel subducts. If the PV is conserved and low PV anomalies are subducted (Gent & McWilliams, 1990), the stratification on the parcel will increase and the parcel will develop more anticyclonic vorticity as the water parcels subduct (Wang, 1993; Spall, 1995). This analysis of vortex stretching ignores the horizontal components of the PV, q_h which may be significant in areas with strong lateral density gradients. If q_h becomes increasingly negative during subduction, then ζ may not decrease as much as would be expected from (11).

In what follows, we draw on concepts from the diagnostic semigeostrophic Omega equation, as well as conservation of PV, to better understand the subduction of water masses from the mixed layer to the interior.

4 Methods

A three-dimensional numerical model is used to explore the dynamical mechanisms for subduction from the mixed layer into the pycnocline in the absence of strong surface

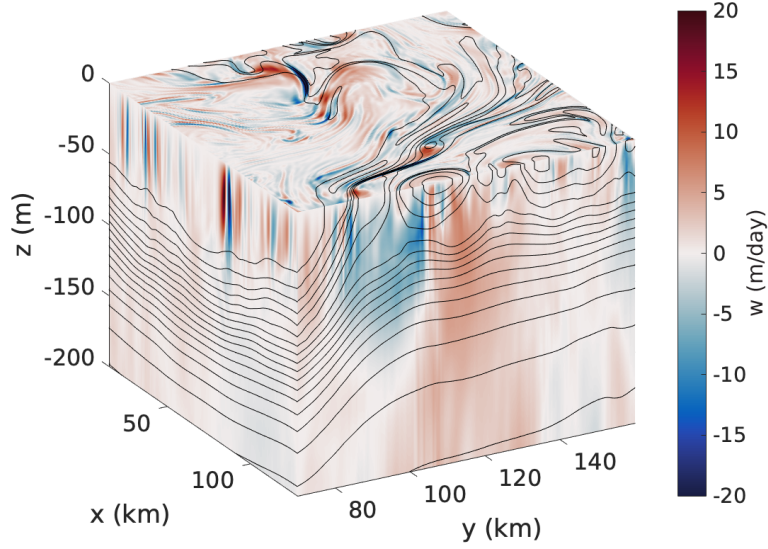


Figure 2. Vertical velocity with density contours on day 47.5. The vertical velocity that is shown at the surface is the 5 meter vertical velocity. Vertical velocity is shown in meters/day, with a saturated color scale.

forcing (wind stress or cooling). Our strategy is to follow water parcels and track their properties as they are subducted. By analyzing the kinematic and hydrographic properties in the Lagrangian frame as water parcels are subducting, we aim to statistically identify the characteristics and evolution of different subduction events.

4.1 Model set up

We simulate a front using the non-hydrostatic Process Study Ocean Model (PSOM) (Mahadevan et al., 1996a, 1996b; *PSOM*, 2020) in a zonal periodic channel. In the meridional direction, the model is initialized with the observed pycnocline structure of the mesoscale front on the edge of the Eastern Alborán Gyre in the Western Mediterranean and a 50-70 meters deep mixed layer, typical of late-winter and early-spring conditions. The initial condition has a small-amplitude meander with one wavelength in the zonal direction to nudge the model to develop the large-scale meandering structure that is observed in the Alborán Sea. The model domain is centered at 36.9°N. The inertial period is 20 hours.

The model domain extends 128 km in the (periodic) x -direction and 206 km in the y -direction (with closed walls) and 1000 m in depth. The horizontal resolution is 500 meters, with a stretched grid in y that attains a spacing of 2 km within 40 km of the south-

ern and northern solid boundaries. There are 64 vertical levels on a stretched grid with grid spacing ranging from 0.5 m at the surface to 54 m at depth. The model timestep is 108 seconds. The horizontal diffusion is $1 \text{ m}^2/\text{s}$. The vertical diffusion has a constant value of $10^{-5} \text{ m}^2/\text{s}$. The model has a flat bottom and a linear bottom drag of 10^{-4} m/s . The model forced with weak cooling at a rate of 15 W/m^2 at the surface to maintain the mixed layer. The density is adjusted to a stable state by convective adjustment.

4.2 Particle tracking

Particle trajectories are used to identify subduction locations and study the evolution of dynamical properties along water parcel trajectories. Particles are advected offline from the model integration of momentum using an implementation of the Vries and Döös (2001) particle advection algorithm in Python (Dever & Essink, 2020). The particles are advected using instantaneous velocity fields from the three-dimensional model saved every 3 hours and interpolated linearly to intermediate times. Particle trajectories integrated offline for 10 days (with 3-hourly model output) do not differ significantly from those calculated online in the model. For our study, we seed 12,700 each day at a spacing of 1 km at 5 meters depth from model days 44 to 62. A total of 228,600 particles are used in this study. Tracers and velocities are interpolated from the model grid onto the particle positions using tri-linear interpolation. All gradients are computed on the model grid and then interpolated onto the particle positions.

4.3 Tracers

Similar to the particles, we advect 2 tracers offline with the model's advection routine and a time step of 108 seconds, using the 3-hourly model velocity fields interpolated in time.

A mixed layer tracer is used to diagnose the subduction rates and validate the particle results (Figure ??). This tracer is initialized with a value of 1 in the mixed layer and 0 outside the mixed layer. At every time step, the tracer concentration is instantaneously restored to 1 in the mixed layer, but not restored below the mixed layer.

A depth tracer is used to calculate the vertical transport rate over a time interval Δt . Since the tracer is continuous, it allows us to calculate variance spectra of the vertical transport rate as a function of horizontal wavenumber. The depth tracer is initialized on model day 43.75 (time t_0) with a value that equals its vertical position z , such that $Tr(x, y, z, t_0) = z(t_0)$. The vertical transport rate ($w^{\Delta t}$) over a time interval Δt is computed as the difference between the tracer value at $t_0 + \Delta t$ and t_0 as

$$w^{\Delta t} = \frac{Tr(x, y, z, t_0 + \Delta t) - Tr(x, y, z, t_0)}{\Delta t} \quad (12)$$

The two-dimensional (x - y) isotropic spectra of $(w^{\Delta t})^2$ is computed using the package *pyspec* (Rocha, 2015).

5 Results

5.1 Subduction rate

The model domain contains a front within the pycnocline, with frontal isopycnals outcropping in the mixed layer, which ranges from 70 m on the light side of the front to 50 m on the dense side of the front. During the spin up phase, the front first develops mixed layer submesoscale instabilities. The mixed layer depth (defined as where the local density exceeds the surface density by 0.0125 kg/m^3) shoals to as little as 5 meters along the front, but maintains a depth of 50–70 meter away from the front. By day 20, mesoscale baroclinic instability develops (Figure 2). This progression of instabilities is consistent with previous studies on linear unstable modes: a smaller-scale, faster growing mixed layer mode and a larger scale pycnocline mode (Boccaletti et al., 2007; Calles et al., 2016). During the analysis period (model days 44 to 62), instabilities at both the mesoscale and submesoscale are present, but the regions where the local Rossby number ($Ro = \frac{U}{fL}$) is large, $Ro \gtrsim 1$, are mostly localized around the mesoscale front.

Mixed layer water subducts into the pycnocline at a rate of 0.2–0.3 Sv over the $82,560 \text{ km}^2$ domain over course of the analysis period. The subduction rate is computed as the rate of change of the volume of mixed layer water present below the mixed layer and amounts to 25 m of the mixed layer being subducted over a 3-month period (the approximate duration of the winter and early spring conditions simulated here). The subduction rate is diagnosed using a mixed layer tracer, initialized with a value of 1 in the mixed layer and zero below the mixed layer. At each time step, the tracer concentration is restored to 1 in the mixed layer using the updated density fields, and not restored below the mixed layer. The mixed layer depth is defined as a density difference from the surface of $\sigma = 0.0125 \text{ kg/m}^3$.

5.2 Coherent subduction

In the Lagrangian analysis, we consider subduction to occur when a water parcel that was initially in the mixed layer, moves 5 meters below the mixed layer. We identify the water parcel’s subduction location (horizontal position) and time (model day) (Figure 3). The mixed layer depth (estimated by a density threshold of 0.125 kg/m^3) is interpolated onto the particle locations at every time step. Of all of the particles seeded evenly across the domain at 5 meters and reseeded daily, 7.7%, or 18,740, subduct out of the mixed layer in localized regions along the front.

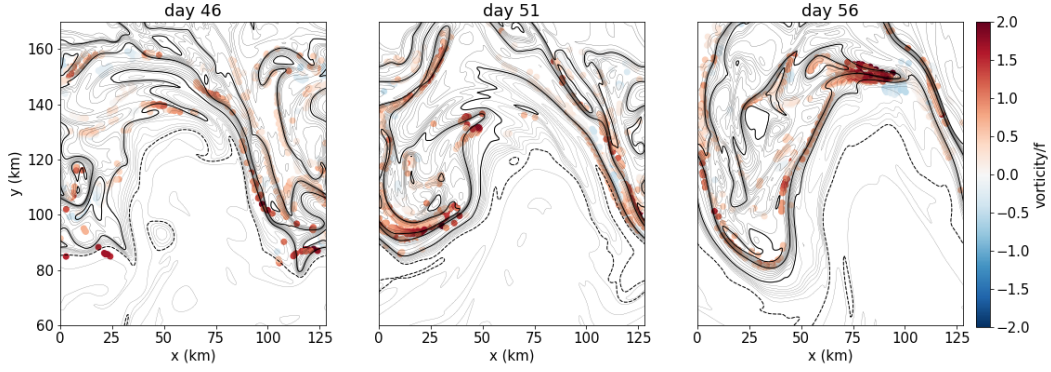


Figure 3. Positions (x - y) of particles on the day that they subduct out of the mixed layer.

The particles are colored by their relative vorticity, with red referring to cyclonic, and blue to anti-cyclonic vorticity. Density at 5 m depth is contoured (thin lines $CI = 0.02 \text{ kg/m}^3$, thick lines $CI = 0.2 \text{ kg/m}^3$). Dashed (solid) contours are lighter (denser) than the average surface density. Particles are subducting along the dense side of the fronts where the lateral buoyancy gradient is strongest, and most of the particles have cyclonic relative vorticity. The subduction locations are coherent and elongated in the along-front direction.

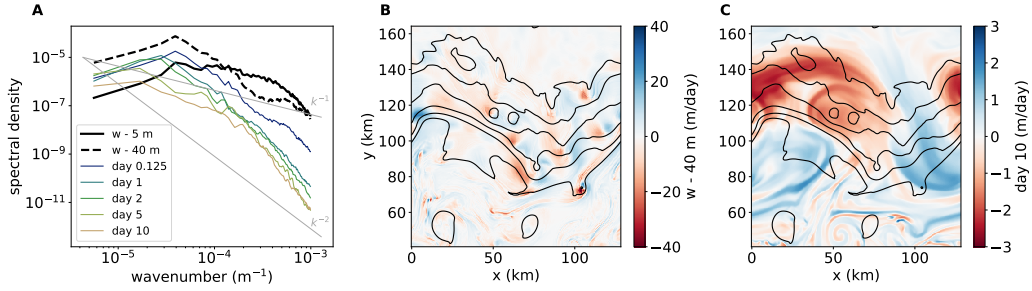


Figure 4. (A) Vertical velocity and vertical transport isotropic wavenumber variance spectra.

The black lines are the vertical velocity spectrum at (solid) 5 meters depth and (dashed) 40 meters depth. The colored lines show the spectrum of the vertical transport calculated over a range of time intervals according to (12) at 40 meters depth. The grey lines are guides for k^{-1} and k^{-2} slopes. (B) Vertical velocity at 40 meters depth. (C) Vertical transport over 10 days at 40 meters depth.

The complex frontal density structure results in a rich variety of features on which water parcels subduct (Figure 3). Subduction occurs at the strongest density gradients, which are outcrops of the front within the pycnocline, and at mixed layer fronts on the dense side of the pycnocline front. The subduction locations are almost all located on the dense side (cyclonic side) of the main pycnocline fronts, but only along some parts of the front, in transient features associated with submesoscale filaments and eddies.

The water parcel subduction locations are spatially coherent; more coherent than either the initial position of water parcels that subducted out of the mixed layer or the final water parcel positions after subduction. We use tracer spectra to quantify the coherence of transport across different spatial and temporal scales (Figure 4). The near-surface (5 m) vertical velocity has variability across a wide range of spatial scales, including small scales, as evidenced by the nearly flat spectrum. Since the vertical velocity goes to zero at the surface, the vertical velocity at 5 meters depth is approximately equal to the surface horizontal divergence multiplied by the depth, Δz ,

$$w \approx \nabla_h \cdot \mathbf{u}_h|_{z=0} (\Delta z). \quad (13)$$

At shallow depths, the vertical velocity spectrum $\langle w^2 \rangle$ is therefore related to the horizontal velocity spectrum $\langle \mathbf{u}_h^2 \rangle$ by

$$\langle w^2 \rangle \sim \langle \nabla \cdot \mathbf{u}_h^2 \rangle \sim k^2 \langle \mathbf{u}_h^2 \rangle. \quad (14)$$

At 40 meters depth, which is near the base of the mixed layer, the vertical velocity spectrum is steeper than predicted by (14) and not directly related to the local divergence of the horizontal velocity near the surface because the divergence has variable magnitude and sign between 40 meters and the surface. The vertical velocity spectrum at 40 meters has a flat spectrum at the smallest scales resolved. The spectrum of the vertical transport defined by (12) has lower power than the vertical velocity spectrum at all scales because it is time integrated. The instantaneous vertical velocity has more extreme values than the time integrated vertical transport. Over time intervals of less than one day, the transport spectrum differs more from the vertical velocity spectrum at high wavenumbers (small spatial scales). Much of the difference is due to the influence of internal waves on the vertical velocity spectrum but not the transport spectrum (Balwada et al., 2018). Over time intervals of 5-10 days, the transport spectrum flattens mostly in the smaller wavenumber range. The result is a relatively flat spectrum at spatial scales from around 100 km to 10 km ($\sim k^{-1}$). This spectral shape suggests that features at scales of tens of kilometers are particularly important for subduction from the surface on timescales of 5-10 days. This is approximately the spatial scale of the coherent features found in the observations.

5.3 Lagrangian analysis of subduction by frontogenesis

Subduction is characterized from a Lagrangian perspective by compositing dynamical properties on a shifted time axis with time zero being the day on which the water parcel was subducted. Figures 5 and 6 show the Lagrangian time evolution of properties on the water parcels that are subducted out of the mixed layer. The solid line is the median of each property (lateral and vertical density gradients, relative vorticity, vertical velocity, PV, cyclostrophic acceleration, and frontogenesis terms) and the shaded region is the interquartile range. The properties on half of the subducting particles fall within the interquartile range, but half fall outside this range. The median of the dynamical properties on the quickly subducting water parcels (water parcels that reach at least 20 m/day downward vertical velocity) is shown in the dashed line. The time prior to subduction when particles are in the mixed layer is indicated as negative, time zero represents a transition as particles subduct, and the positive time axis shows the period of their evolution after subduction. The evolution of the water parcel properties during subduction sets the properties of the subducted water masses. As expected for downward motion from the mixed layer to the pycnocline, the stratification (N^2) increases (Figure 5A) and the vertical velocity increases in magnitude (downwards) (Figure 5B). The ratio of the magnitude of the lateral to vertical buoyancy gradient, M^2/N^2 , is the isopycnal slope. The isopycnal slope is large in the mixed layer and during subduction, which mostly occurs along steeply sloping isopycnal surfaces (M^2 and N^2 both increase). The stratification continues to increase as water parcels subduct, but the lateral buoyancy gradient peaks during subduction and then gradually decreases (Figure 5A) as subducted water parcels enter a region of higher stratification. This restratification on a Lagrangian trajectory does not necessarily mean that the larger-scale front restratifies. Instead, water parcels are moving along density surfaces into a more stratified region. The mixed layer volume stays relatively constant and does not decrease throughout the analysis period (Figure ??).

The intensification of the lateral buoyancy gradient prior to and during subduction demonstrates that frontogenesis plays an important part in subduction (Figure 5A). The Lagrangian rate of change of the lateral buoyancy gradient following a water parcel is the frontogenetic tendency. On average, frontogenesis occurs here due to straining by the geostrophic velocities. The ageostrophic strain also contributes to average frontogenesis during subduction (Figure 6A; Equation 2). After subduction, frontolysis is mainly due to the ageostrophic overturning circulation and horizontal diffusion (Figure 6A).

Concurrent with frontogenesis, the vertical component of the relative vorticity increases rapidly on water parcels as they approach the subduction location, after which their relative vorticity decreases (Figure 5B). Nearly all of the water parcels have cyclonic

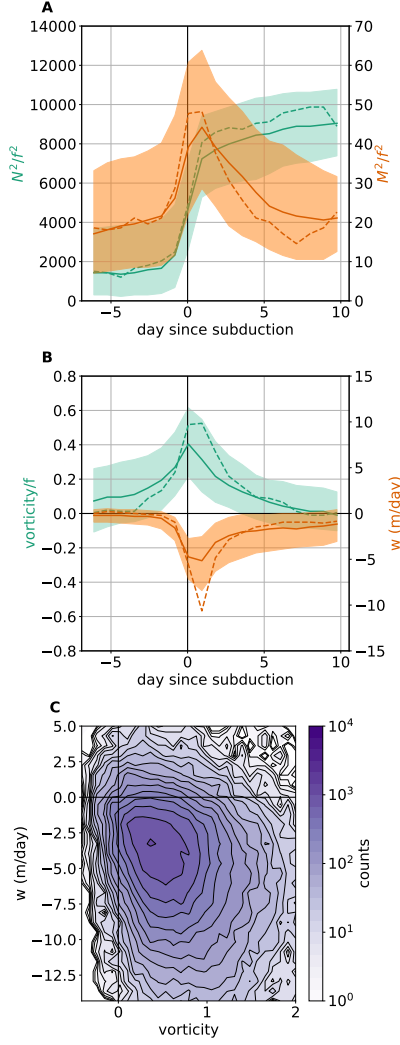


Figure 5. Lagrangian evolution of dynamical quantities as water parcels are subducted. All trajectories are composited onto a shifted time axis where time zero is the subduction time of the water parcel (defined as the time when it moves from the mixed layer to 5 meters below the mixed layer depth). The solid line is the median value. The shaded region encloses the first and third quartiles of all subducted particles. Approximately 7% of all of the particles subduct. The dashed line shows the median of all particles that subduct faster than 20 m/day. (A) Stratification (N^2/f^2) (left axis, green) and lateral buoyancy gradient (M^2/f^2) (right axis, orange) (B) Relative vorticity normalized by the Coriolis frequency (left axis, green) and vertical velocity (right axis, orange) (C) Two dimensional histogram showing the relationship between the vertical component of relative vorticity (normalized by f) and the vertical velocity on particles during the 20 hours prior to subduction. The reference Coriolis frequency used to normalize properties is $f = 10^{-4} \text{s}^{-1}$.

vorticity when they initially subduct out of the mixed layer and about half develop anticyclonic vorticity by the end of the trajectory (Figures 5B and 3). The third quartile of relative vorticity on subducting water parcels reaches $\sim 0.6f$. The average rate of subduction on trajectories is fairly slow, at 1–4 meters per day. However, the vertical velocity during and immediately after subduction can be large (20–30 m/day). A joint distribution of vertical velocity and vertical component of the relative vorticity at the time of subduction reveals that the relative vorticity and vertical velocity are negatively correlated, but the largest values of vertical velocity have a significant range of relative vorticities (Figure 5C). The peak of the vorticity leads the peak of the downward vertical velocity (Figure 5B) due to the relationships between vorticity and vertical velocity. At the sea surface, vertical velocities approach zero but relative vorticity often reaches a maximum; vortex stretching is due to the vertical shear of the vertical velocity. As water parcels subduct, they enter a region of larger downward vertical velocity. Furthermore, the curvature on the trajectories may generate the downwelling vertical velocity. The large values of cyclonic vorticity on the dense side of the front contribute to strengthening the PV gradient and make the front susceptible to baroclinic and barotropic instabilities that manifest as frontal waves. The increase in cyclonic vorticity on the water parcels is due to two factors: (i) shear on the edge of the jet, which is a 2D mechanism (cross front and in the vertical) and is described by the semi-geostrophic Omega equation, and (ii) curvature of the trajectories, a 3D process that includes along-front variability and impacts the dynamics through a cyclostrophic acceleration, $\frac{V^2}{R}$ where V is the velocity magnitude and $R = \frac{(u^2+v^2)^{3/2}}{uv_t-vu_t}$ is the radius of curvature. If the cyclostrophic term is the same order of magnitude as the Coriolis term, the balanced velocity will be in gradient wind balance, rather than geostrophic balance. The cyclostrophic term is larger when the flow is more non-linear. On the particle trajectories, the cyclostrophic acceleration increases prior to subduction, peaks 2–3 days after subduction on average, and then decreases (Figure 6B). The water parcels have cyclonic vorticity during subduction, so the cyclostrophic term decelerates the velocity relative to the geostrophic velocity. This deceleration results in a convergence and downwelling along the particle trajectories. In this way, the spiralling of water parcels helps to maintain downward transport.

The Ertel potential vorticity (PV; equation 10) is conserved on the water parcels except during the subduction event, indicating that diabatic processes play a part in the subduction process. In the mixed layer, the PV is near zero due to the low stratification or, at strong fronts, slightly negative due to the negative contribution from the product of the horizontal buoyancy gradient and horizontal component of vorticity. During subduction, the total PV on the water parcels increases nearly as a step function (Figure 6C). The PV can be split into a vertical (vortical) contribution (q_v) and a horizontal (baro-

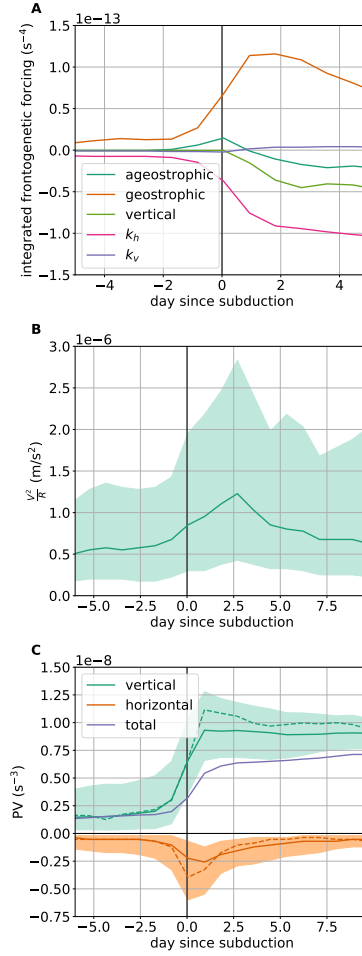


Figure 6. Evolution of dynamical quantities as particles are subducted. All particle trajectories are composited. Quantities are averaged on a shifted time axis where time zero is the subduction time (defined as the time when particles move from the mixed layer to 5 meters below the mixed layer depth). The solid line is the median value. The shaded region encloses the first and third quartiles of all subducted particles. (A) Contributions to frontogenesis split into the terms on the right hand side of Equation 2. The forcing due to each term is integrated in time along each particle trajectory. The lines show the median of the integrated frontogenetic forcing on all particles on a shifted time axis. Positive values are frontogenetic and negative values are frontolytic. The \mathbf{Q} -vector is split into geostrophic and ageostrophic components. The third term is frontogenesis by the vertical velocity (“vertical”). The fourth term is horizontal diffusion (k_h). The fifth term is vertical diffusion (k_v). (B) Non-linear acceleration on the particle trajectories. The radius of curvature (R) is calculated using velocities and accelerations averaged over 15 hours on particle trajectories. (C) Vertical and horizontal contributions to the PV. The dashed line shows the median of all particles that subduct faster than 20 m/day. The black line is the median of the total PV.

clinic) contribution (q_h). q_v remains elevated once the water parcels have subducted. The magnitude of q_h , which is negative, increases transiently as the water parcels subduct. The increase in the magnitude of q_h and decrease in the vertical component of relative vorticity (ζ) does not balance the increase in q_v that arises from an increase in stratification, N^2 (Figure 5A). The mixed layer tracer also reveals a slight increase in PV during subduction in this model (Figure ??).

5.4 Submesoscale subduction

The coherence of the modeled subduction on submesoscale length scales and the large localized Rossby number at the time of subduction suggests that submesoscale dynamics enhance subduction. Examining particle trajectories on isopycnal surfaces reveals some of these submesoscale processes. While some water parcels stay close to the mixed layer base after subducting, features with 10 km scales transport water parcels vertically and horizontally away from the front, potentially leading to longer term subduction.

Submesoscale features contribute to subduction through both restratification and along isopycnal stirring. Restratification and along isopycnal stirring may work in tandem to promote subduction. In a typical scenario, restratification will happen most quickly at the surface and at the mixed layer base (Fox-Kemper et al., 2008). Once the mixed layer base restratifies, water parcels are trapped in a transition layer with reduced turbulence. Water parcels are then less likely to be reentrained by mixed layer turbulence and can subduct along isopycnal into the pycnocline. These transition layers have been observed (Shcherbina & D’Asaro, 2020) and modeled using large eddy simulation (LES) (Taylor et al., 2020).

Along-isopycnal subduction varies with depth. Lighter (shallower) isopycnal surfaces have relatively low and homogeneous PV with small scale PV gradients suggesting along isopycnal stirring of PV (Figure 7E,F). By contrast, on a denser (deeper) isopycnal surface, there is a much clearer PV gradient with low PV mostly confined near the surface, although below the mixed layer, with some low PV filaments at depth (Figure 8G,H). The denser surfaces span a large depth range and so have more potential for deep and rapid subduction.

Mesoscale meanders generate strain, which results in frontogenesis and downwelling on the portion of the front leading into the trough of the meander and frontolysis with upwelling leading into the crest of the meander (Bower et al., 1985; Bower, 1991; Samelson, 1992). The vertical velocity due to the mesoscale meander straining itself has a vertical structure corresponding to that of the first baroclinic mode, which depends on the stratification. The first baroclinic mode typically has a maximum in the main thermocline and decreases towards the surface. Due to this vertical and horizontal structure,

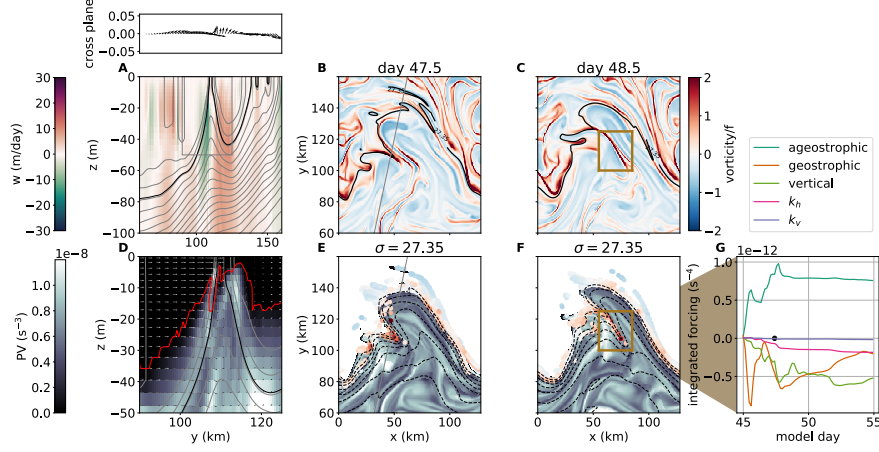


Figure 7. A submesoscale filament as a pathway for subduction from the mixed layer. (A, D) Cross section on day 47.5 at the grey line on panels (B, E). Contours are isopycnals with $\sigma = 27.35$ as a bold line. (A) Upper panel: surface horizontal velocity along the line in Panels B and E. Downwards is out of the page with respect to Panels A and D. Lower panel A: Vertical velocity in meters per day. D: PV with velocity vectors. The red line is $Ri = 0.7$. This panel shows a subsection of the previous panels, the extent of which is outlined in the grey box in panel (A). The evolution of a cyclonic filament is shown over two days in panels (B,C,E,F). (B,C) surface relative vorticity normalized by the Coriolis frequency. The thick contour is $\sigma = 27.35$. (E,F) PV on the $\sigma = 27.35$ surface. The black contours are isopycnal height at 10 meter intervals. All particles shown have density within 0.01 kg/m^3 of the isopycnal surface and subduct below the mixed layer during their trajectory. The particles are colored with their relative vorticity. (G) Contributions to frontogenesis split into the terms on the right hand side of Equation (2). The forcing due to each term is integrated in time along each particle trajectory. The lines show the mean of the integrated frontogenetic forcing on all particles within the brown box in panel F. Positive values are frontogenetic and negative values are frontolytic. The black dot on the x-axis denotes the subduction time.

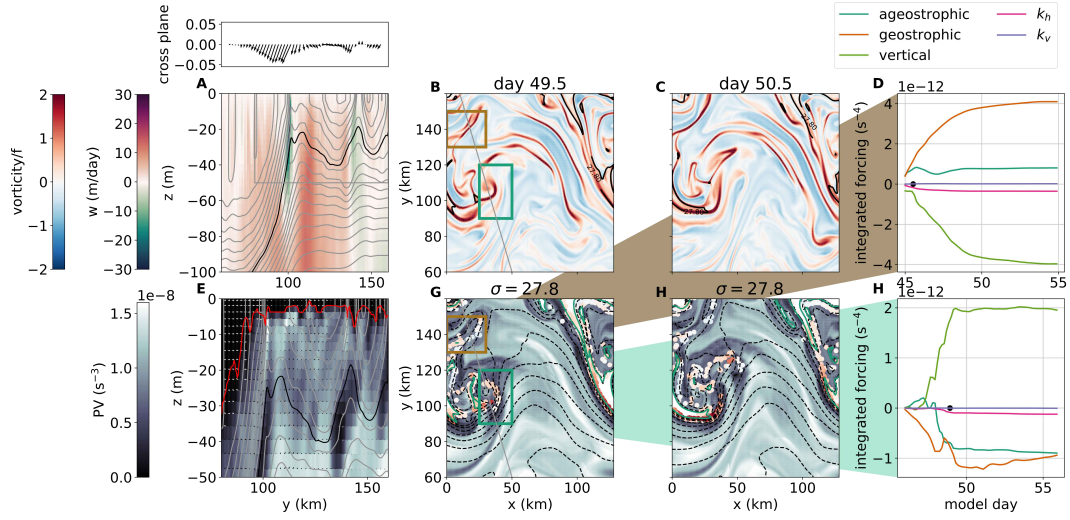


Figure 8. Two specific pathways for subduction from the mixed layer. (A, DE) Cross section on day 49.5 at the grey line on panels (B, G). Contours are isopycnals. The black contours $\sigma = 27.8$. (A) Upper panel: surface horizontal velocity in the along plane direction (x-axis) and cross plane direction. Downwards in the cross plane direction is out of the page (positive x direction). Lower panel: Vertical velocity in meters per day (D) PV with velocity vectors. This panel shows a subsection of the previous panels, the extent of which is outlined in the grey box in panel (A). The evolution of a cyclonic filament is shown over two days in panels (B,C,G,H). (B,C) surface relative vorticity normalized by the Coriolis frequency. The thick contour is $\sigma = 27.8$. (G,H) PV on the $\sigma = 27.8$ surface. The black contours are isopycnal height at 10 meter intervals. All particles shown have density within 0.01 kg/m^3 of the isopycnal surface and subduct below the mixed layer during their trajectory. The particles are colored with their relative vorticity. (D, H) Contributions to frontogenesis split into the terms on the right hand side of Equation 2. The forcing due to each term is integrated in time along each particle trajectory. The lines in D and H show the mean of the integrated frontogenetic forcing on all particles within the brown box in panel G (panel D) and the green box in panel G (panel H). Positive values are frontogenetic and negative values are frontolytic. The black dot on the x-axis is located at the subduction time.

the mesoscale meander results in slow and relatively large scale (80-100 km in this scenario) subduction. In addition to this contribution to subduction, the mesoscale meander, and particularly its along-front structure, provides a setting for the growth of dynamically different submesoscale features that lead to subduction on smaller scales. In what follows, we describe three such submesoscale features causing subduction.

5.4.1 *Intrapycnocline eddies*

Quasigeostrophic theory predicts that subduction occurs due to geostrophic frontogenesis, which generates ageostrophic horizontal and vertical velocities. As low PV surface mixed layer water crosses the front it subducts along an isopycnal surface while conserving quasigeostrophic PV, $q = \frac{f+\zeta}{H}$, where H is the layer thickness. If the mixed layer is thicker than isopycnal layers in the thermocline, the subducted water mass becomes an anticyclonic intrapycnocline eddy as it is compressed during subduction (Spall, 1995). The length scale of the intrapycnocline eddy is expected to be the internal deformation radius. The radius of deformation of the mixed layer is $\frac{N_0 D}{f} \approx 3$ km where $N_0^2 = 10^{-4} \text{ s}^{-1}$ is the reference stratification, $D = 30$ m is the mixed layer depth, and $f = 10^{-4} \text{ s}^{-1}$.

Multiple intrapycnocline eddies are identified in cross sections as low PV anomalies (Figure 8E) with radii slightly larger than 3 km. The formation of a low PV intrapycnocline eddy on the $\sigma = 27.8$ isopycnal surface is highlighted in the brown box in Figure 8B,G. The water parcels that become the intrapycnocline eddy subduct from a region of large cyclonic vorticity on the meander branch leading into the trough due to geostrophic frontogenesis with some contribution from ageostrophic frontogenesis (Figure 8D). The water parcels subduct on a dense (cyclonic) filament that outcrops at the center of the front. The intra-pycnocline eddy that forms during subduction moves towards the dense side of the front and is elongated as it subducts into a region where the vertical branch of the ageostrophic circulation is frontolytic. The water parcels, which initially have large values of cyclonic vorticity, develop anticyclonic vorticity within one day. The intrapycnocline eddy has a cyclonic surface expression.

Intrapycnocline eddies have been observed near fronts (Archer et al., 2020) and anticyclonic submesoscale vortices with likely generation at fronts have been observed more generally. These eddies trap material in the interior and are potentially important for transporting heat, salt, and biological communities (Frenger et al., 2017). In this study, we observe that the subducted water masses fill the center of the subducted feature, supporting their role in material transport.

5.4.2 *Submesoscale filaments*

As the vorticity rapidly increases at the mesoscale front due to geostrophic frontogenesis, the front develops wave-like features at the sharpest density gradient (Figure 7B,C). The frontal wave appears to have developed due to the co-occurrence of large horizontal shear and baroclinicity. The fronts on these waves further intensify due to ageostrophic circulations. As these waves grow, they may wrap up in submesoscale vortices or elongate into filaments.

An example of a filament generated by geostrophic and ageostrophic frontogenesis is shown in Figure 7E,F. The large cyclonic relative vorticity and low Richardson number is present throughout the 40 m mixed layer (Figure 7A). Prior to subduction, ageostrophic and geostrophic frontogenesis increases the density gradients (positive slopes in integrated frontogenetic forcing), generating a cyclonic filament. Water parcels subduct out of the mixed layer during the development of the filament. There is upwelling on either side of the subduction region that brings up high PV water. This high PV water and strong buoyancy gradients are mixed into the subduction region. This results in a subducting water mass that has high PV relative to its isopycnal surface. After subduction, the water parcels are transported more than 80 km laterally across the domain and continue to subduct as the cyclonic filament relaxes. This example reveals a pathway to subduct anomalously high PV attained through diapycnal mixing with surrounding water.

Here, (Figure 7G) the filament intensifies by both geostrophic and ageostrophic frontogenesis (Barkan et al., 2019) and decays due to geostrophic frontolysis, horizontal diffusion and vertical transport. Other model studies with 500 m resolution but smaller horizontal diffusivity and boundary layer turbulence parameterized by KPP, have found that filamentogenesis is halted by secondary instabilities of the filament rather than by diffusion (Gula et al., 2014; Barkan et al., 2019), in contrast to lower resolution models (1.5 km). Additional submesoscale subduction might be expected on a filament due to secondary instabilities in a simulation where they are present.

Previous observational and modeling studies have shown that cold (cyclonic) submesoscale filaments can contribute to exchange between the surface and pycnocline in the Gulf Stream and Antarctic Circumpolar Current (Gula et al., 2014; Klymak et al., 2016; Taylor et al., 2018).

5.4.3 *Cut-off cyclones*

Low PV water masses are also transported below the mixed layer through generation of a cyclone (Figure 8G, green box). The mixed layer base, not just the sea surface, is involved in the formation of the submesoscale cyclone as differential vertical mo-

tion tilts the stratification at the mixed layer base onto the horizontal (Figure 8H). As a consequence of the frontal waves, the core of the submesoscale cyclone is light, rather than dense as is typical of a cyclonic eddy. The cyclonic vorticity is largest on the edges rather than the center of this eddy (Figure 8B). The core of the submesoscale cyclone has high PV, rather than the low PV that would be expected from an intrapycnocline eddy. Low PV mixed layer water parcels leave the mixed layer around the edges of the cyclone. While subduction is 3D in the surface layer, once water parcels leave the mixed layer, they are transported along isopycnal surfaces and the subduction has a more 2D character. This subduction results in a low PV water mass at depth that has weakly cyclonic vorticity (Figure 8E, near 100 km). The length scale of this subducted region is set by the wave length of the frontal waves. The modeled cyclone does not cross to the light side of the mesoscale front and instead is deformed by the mesoscale flow. The low PV water mass does not become a submesoscale coherent vortex and the length scale of the low PV water subsurface is determined by stirring.

The dynamics and kinematics of the modeled cyclone reflect the formation process of cutoff cyclones, or cutoff lows, in atmospheric dynamics (Rotunno et al., 1994). Cutoff lows are known to be important for stratosphere-troposphere exchange (Holton et al., 1995; Fuenzalida et al., 2005). Related dynamics in the ocean may naturally be expected to be relevant for exchange between the mixed layer and thermocline. A similar feature to the modeled cyclone was observed in a section across the western Alborán Gyre (Figure 1B,C).

6 Discussion

Observations show that coherent subducted water masses are ubiquitous at strong fronts (Thomas & Joyce, 2010; Pascual et al., 2017). We describe and analyze a range of subduction processes that generate observed subsurface intrusions and describe characteristics that might aid diagnosis of these processes from observations. The subduction, which arises from coupled mesoscale and submesoscale dynamics, is mostly localized at the strong mesoscale front, but occurs episodically along that front due to frontogenetic processes with high spatial and temporal variability. By analyzing the trajectories of water parcels we find that submesoscale features generated through baroclinic instability of the mesoscale front open pathways into the interior. Even in locations of net mesoscale upwelling, submesoscale dynamics subduct water from the mixed layer resulting in subduction that is coherent on spatial scales of order 10 km. These results suggest that the coherent transport from the surface to the interior observed in cross-front transects in the Western Mediterranean and other locations globally could be the result of baroclinic instabilities of the mesoscale front.

The density structure of the front determines the potential for subduction from the mixed layer to the interior. When density surfaces extend from the pycnocline into the mixed layer, water parcels can subduct along an isopycnal surface into the pycnocline. Water parcels on density surfaces that do not extend into the pycnocline may leave the mixed layer through restratification, for example by mixed layer instability. Almost all of the water parcels in this study subduct on the dense side of the front, on isopycnals that extend into the pycnocline.

Subduction patterns are largely driven by along-front variability of the meander, which plays an important role in generating ageostrophic secondary circulations through frontogenesis and is shaped by those same ageostrophic secondary circulations (McWilliams et al., 2019). Subduction from the mixed layer is the result of vertical velocity generated due to a range of processes, including geostrophic and ageostrophic frontogenesis at the surface, and vertical motion due to frontogenesis at the mixed layer base. The presence of the mesoscale front may in some situations enhance submesoscale instability (Rotunno et al., 1994) but mesoscale fronts may also stabilize the flow through strain or barotropic shear (Gula et al., 2016; Taylor et al., 2018; Stamper et al., 2018). The cyclonic curvature of water parcel trajectories that encounter frontal waves also leads to gradient wind balanced velocities that modify the ageostrophic overturning. Along-front variability in both horizontal and vertical velocity patterns breaks the periodicity of the meander, resulting in longer-term subduction. The mesoscale meander structure studied here provides a distinct scenario from previous studies and reveals many ways in which submesoscale and mesoscale processes are coupled.

While the frontogenesis and subduction is on average geostrophic in this study, we outline the importance of ageostrophic and three-dimensional processes for subduction and illustrate these subduction processes with specific examples. Submesoscale cyclonic vortices and filaments are common due to instabilities or frontal waves in the model and in observations. We show that these features make important contributions to subduction. Frontal waves and eddies that are qualitatively similar to those that contribute to the rapid subduction in the case studies presented here have been observed previously, mostly from satellites and photographs from space shuttles, and have been attributed to both shear instability and baroclinic instability (Munk et al., 2000; Yin & Huang, 2016; Klymak et al., 2016). In both cases, the waves are observed to go unstable in 2-3 days and have wavelengths of 20-30 km, consistent with the modeled features. Once a shear instability develops, the waves result in increased lateral density gradients that can generate submesoscale features and rapid subduction through ageostrophic frontogenesis (Rotunno et al., 1994; McWilliams et al., 2015). Additional three-dimensional processes beyond ageostrophic and vertical frontogenesis play important roles in subduction. Both the cy-

625 clostrophic acceleration (McWilliams et al., 2019) and the conversion from the baroclinic
 626 to the vortical contributions of the PV (Thomas, 2008) reveal the importance of along-
 627 front curvature in driving subduction.

628 Submesoscale subduction occurs in regions along the mesoscale front and subme-
 629 soscale features transport water parcels deeper and farther from the front laterally than
 630 mesoscale subduction. The small spatial scale of coherence results in subducted features
 631 that persist on time scales of tens of days. The spatial scale of the subduction affects the
 632 upper ocean thermohaline structure (Cole & Rudnick, 2012; Spiro Jaeger, 2019) and bio-
 633 geochemical tracer distributions (Erickson & Thompson, 2018). The coherence of the
 634 subduction has implications for the timescales of the subduction. If the subduction were
 635 completely incoherent it could be appropriately modeled as a diffusive process. If sub-
 636 duction took place through a steady overturning process, it would either be completely
 637 reversible or only associated with restratification. Geostrophic frontogenesis can gener-
 638 ate submesoscale coherent vortices subsurface. These vortices trap material and can move
 639 long distances away from the front (Frenger et al., 2017). These vortices represent a non-
 640 local subduction process. By contrast, the cut-off cyclone generated by along-front vari-
 641 ability subducts material on the edges of the submesoscale cyclone. This material is stirred
 642 along the isopycnal surface after subduction and does not remain coherent for as long.

643 The largest values of vertical velocity in this simulation are 30-40 meters/day. Stronger
 644 submesoscale vertical velocities have been both observed and modeled (Mahadevan et
 645 al., 2010; D’Asaro et al., 2018). The vertical velocity can be expected to be stronger in
 646 model situations with wind forcing, with a boundary layer turbulence parameterization,
 647 deeper mixed layer, stronger mesoscale jet, and with a smaller value of horizontal eddy
 648 diffusivity (Wang, 1993). In these situations with stronger vertical velocity, the ageostrophic
 649 velocities would also be expected to be stronger. Consequently, ageostrophic frontoge-
 650 nesis and vertical frontogenesis may make a larger contribution to subduction out of the
 651 mixed layer. The vertical frontogenesis mechanism involves frontogenesis of the mixed
 652 layer base. This interaction between the surface and mixed layer base that generates the
 653 submesoscale cyclones could be especially important in simulations with stronger ver-
 654 tical velocities (Rotunno et al., 1994). Away from strong mesoscale fronts, mixed layer
 655 instability could be an important driver of subduction (Boccaletti et al., 2007; Omand
 656 et al., 2015). In such cases where the mixed layer has strong lateral buoyancy gradients,
 657 submesoscale dynamics dominate the flow field, resulting in a “submesoscale soup” con-
 658 sisting of small scale features with high vorticity (Shcherbina et al., 2015; McWilliams,
 659 2016). With stronger surface forcing, symmetric instability could also be an important
 660 contributor to subduction (Thomas et al., 2013; Erickson & Thompson, 2018).

In the composite trajectory and in the cases examined, the lateral buoyancy gradient, M^2 , peaks as the water parcel is subducting out of the mixed layer. The frontolysis processes have to do with the water parcel leaving the mixed layer and entering the region where ageostrophic circulation weakens the lateral density gradients and with diffusion. Improved representation of the frontal arrest process (Bodner et al., 2020) and boundary layer turbulence (Gula et al., 2014) could have large implications for exchange between the mixed layer and interior.

Eddy fluxes at the meso- and submeso-scale are increasingly recognized as important for the transport of water masses and biogeochemical tracers from the surface to the interior (Omand et al., 2015; Balwada et al., 2018; Canuto et al., 2018; Resplandy et al., 2019). Our diagnosed subduction rate of 25 m over a 3-month period representative of the late winter season is consistent with past mesoscale and submesoscale resolving simulations (Gebbie, 2007; Canuto et al., 2018). The diagnosed rate is equivalent to approximately 100 m/year if the same conditions persisted all year. This annual rate is comparable to subduction driven by the large scale mixed layer pump (Gebbie, 2007). This supports the importance of submesoscale eddy processes for subduction. Submesoscale processes will be most important during times of the year and in locations with deep mixed layers, namely the winter and early spring. The seasonal restratification of the mixed layer is an important process for subduction of carbon and oxygen into the interior, but only affects oxygen and carbon transport on annual timescales if the water parcels are transported below the deepest wintertime mixed layer (Palevsky & Nicholson, 2018). Since the submesoscale subduction studied here transports water masses across the mixed layer base without restratifying the mixed layer, it provides a mechanism for transport of water masses below the deepest mixed layer on interannual timescales. The Lagrangian analysis demonstrates the ways in which long term subduction can occur even from spatially and temporally episodic subduction locations. While subduction locations may be short lived and the residence time in subduction locations very short, water parcels that subduct move laterally by ten to hundred kilometers and are not reentrained after subduction. This process study also reveals the challenge of separating submesoscale and mesoscale processes, which may feedback on each other. Mixing across the mixed layer base is important for determining mixed layer and pycnocline oxygen and nutrient budgets. Improved process level understanding of exchange across the mixed layer base could lead to improved estimates of upper ocean productivity and pycnocline ventilation (Jin et al., 2007; Llanillo et al., 2018).

7 Conclusions

Subduction from the surface mixed layer to the interior occurs through the combination of mesoscale and submesoscale processes at a front. Our investigations are carried out without any strong surface forcing. Frontogenesis is the underlying mechanism, and geostrophic frontogenesis is what drives the majority of subduction. Our Lagrangian analysis shows that as water parcels subduct, they experience increased horizontal and vertical buoyancy gradients and a peak in the relative vorticity. A variety of submesoscale features, either cyclonic or anti-cyclonic, support subduction which can occur along high or low PV pathways. Due to the influence of submesoscale along-front variability, subduction from the mixed layer occurs in coherent features with length scales of tens of kilometers. We find that the subduction process is organized by, but not entirely controlled by, the mesoscale meandering jet and is consequently variable, but spatially localized. Subduction locations reflect the large-scale pattern of the mesoscale meander, but display rich spatial and temporal variability. This variability reduces the likelihood of re-entrainment of water parcels into the mixed layer. The dynamical subduction by the submesoscale has a similar subduction rate to the mixed layer pump but is not resolved in global models.

Acknowledgments

We thank Mathieu Dever and Sebastian Essink for providing the particle tracking code, Eric D’Asaro and Jing He for comments on an earlier version of this manuscript, and the Calypso science team for all of the contributions to data collection and for insightful conversations. We especially acknowledge Shaun Johnston for providing the underway CTD data displayed in Fig. 1B,C and Margaret Conley and Mathieu Dever for collaborating on processing the underway CTD data. We thank the captain and crew of the *N/O Pourquoi Pas?* for their invaluable assistance at sea. This research was funded by ONR grant N00014-16-1-3130. MAF was partially funded by a Martin Fellowship from MIT. The codes to reproduce the model and particle runs can be found at <https://doi.org/10.5281/zenodo.3902273> and the code and data to reproduce the figures can be found at <https://doi.org/10.5281/zenodo.4302604> and the links therein.

References

- Archer, M., Schaeffer, A., Keating, S., Roughan, M., Holmes, R., & Siegelman, L. (2020). Observations of submesoscale variability and frontal subduction within the mesoscale eddy field of the tasman sea. *Journal of Physical Oceanography*, 50(5), 1509–1529.

- Badin, G., Tandon, A., & Mahadevan, A. (2011). Lateral mixing in the pycnocline by baroclinic mixed layer eddies. *Journal of Physical Oceanography*, 41(11), 2080–2101.
- Balwada, D., Smith, K. S., & Abernathey, R. (2018). Submesoscale vertical velocities enhance tracer subduction in an idealized antarctic circumpolar current. *Geophysical Research Letters*, 45(18), 9790–9802.
- Barkan, R., Molemaker, M. J., Srinivasan, K., McWilliams, J. C., & D’Asaro, E. A. (2019). The role of horizontal divergence in submesoscale frontogenesis. *Journal of Physical Oceanography*, 49(6), 1593–1618.
- Beaird, N., Rhines, P., & Eriksen, C. (2016). Observations of seasonal subduction at the iceland-faroe front. *Journal of Geophysical Research: Oceans*, 121(6), 4026–4040.
- Boccaletti, G., Ferrari, R., & Fox-Kemper, B. (2007). Mixed layer instabilities and restratification. *Journal of Physical Oceanography*, 37(9), 2228–2250.
- Bodner, A. S., Fox-Kemper, B., Van Roekel, L. P., McWilliams, J. C., & Sullivan, P. P. (2020). A perturbation approach to understanding the effects of turbulence on frontogenesis. *Journal of Fluid Mechanics*, 883.
- Bosse, A., Testor, P., Mortier, L., Prieur, L., Taillandier, V., d’Ortenzio, F., & Coppola, L. (2015). Spreading of levantine intermediate waters by submesoscale coherent vortices in the northwestern mediterranean sea as observed with gliders. *Journal of Geophysical Research: Oceans*, 120(3), 1599–1622.
- Bower, A. S. (1991). A simple kinematic mechanism for mixing fluid parcels across a meandering jet. *Journal of Physical Oceanography*, 21(1), 173–180.
- Bower, A. S., Rossby, H. T., & Lillibridge, J. L. (1985). The gulf stream—barrier or blender? *Journal of Physical Oceanography*, 15(1), 24–32.
- Callies, J., Flierl, G., Ferrari, R., & Fox-Kemper, B. (2016). The role of mixed-layer instabilities in submesoscale turbulence. *Journal of Fluid Mechanics*, 788, 5–41.
- Canuto, V., Cheng, Y., & Howard, A. (2018). Subduction by submesoscales. *Journal of Geophysical Research: Oceans*, 123(12), 8688–8700.
- Cole, S. T., & Rudnick, D. L. (2012). The spatial distribution and annual cycle of upper ocean thermohaline structure. *Journal of Geophysical Research: Oceans*, 117(C2).
- Dever, M., & Essink, S. (2020, 6). *Offline particle tracking*. Retrieved from <https://doi.org/10.5281/zenodo.3902282>
- D’Asaro, E. A., Shcherbina, A. Y., Klymak, J. M., Molemaker, J., Novelli, G., Guigand, C. M., ... others (2018). Ocean convergence and the dispersion

- 766 of flotsam. *Proceedings of the National Academy of Sciences*, 115(6), 1162–
767 1167.
- 768 Erickson, Z. K., & Thompson, A. F. (2018). The seasonality of physically driven
769 export at submesoscales in the northeast atlantic ocean. *Global Biogeochemical*
770 *Cycles*, 32(8), 1144–1162.
- 771 Fox-Kemper, B., Ferrari, R., & Hallberg, R. (2008). Parameterization of mixed layer
772 eddies. part i: Theory and diagnosis. *Journal of Physical Oceanography*, 38(6),
773 1145–1165.
- 774 Freilich, M. A., & Mahadevan, A. (2019). Decomposition of vertical velocity for nu-
775 trient transport in the upper ocean. *Journal of Physical Oceanography*, 49(6),
776 1561–1575.
- 777 Frenger, I., Bianchi, D., Oschlies, A., & Waschowitz, C. (2017). Subsurface coher-
778 ent eddies: Hypoxic stewpots and biogeochemical highways. *EGUGA*, 2236.
- 779 Fuenzalida, H. A., Sánchez, R., & Garreaud, R. D. (2005). A climatology of cut-
780 off lows in the southern hemisphere. *Journal of Geophysical Research: Atmo-*
781 *spheres*, 110(D18).
- 782 Gebbie, G. (2007). Does eddy subduction matter in the northeast atlantic ocean?
783 *Journal of Geophysical Research: Oceans*, 112(C6).
- 784 Gent, P. R., & McWilliams, J. C. (1990). Isopycnal mixing in ocean circulation mod-
785 els. *Journal of Physical Oceanography*, 20(1), 150–155.
- 786 Giordani, H., Prieur, L., & Caniaux, G. (2006). Advanced insights into sources of
787 vertical velocity in the ocean. *Ocean Dynamics*, 56(5-6), 513–524.
- 788 Gula, J., Molemaker, M. J., & McWilliams, J. C. (2014). Submesoscale cold fil-
789 aments in the gulf stream. *Journal of Physical Oceanography*, 44(10), 2617–
790 2643.
- 791 Gula, J., Molemaker, M. J., & McWilliams, J. C. (2016). Submesoscale dynam-
792 ics of a gulf stream frontal eddy in the south atlantic bight. *Journal of Physi-*
793 *cal Oceanography*, 46(1), 305–325.
- 794 Haine, T. W., & Marshall, J. (1998). Gravitational, symmetric, and baroclinic insta-
795 bility of the ocean mixed layer. *Journal of physical oceanography*, 28(4), 634–
796 658.
- 797 Holton, J. R., Haynes, P. H., McIntyre, M. E., Douglass, A. R., Rood, R. B., & Pfis-
798 ter, L. (1995). Stratosphere-troposphere exchange. *Reviews of geophysics*,
799 33(4), 403–439.
- 800 Hoskins, B. J. (1982). The mathematical theory of frontogenesis. *Annual review of*
801 *fluid mechanics*, 14(1), 131–151.
- 802 Hoskins, B. J., & Bretherton, F. P. (1972). Atmospheric frontogenesis models:

- 803 Mathematical formulation and solution. *Journal of the Atmospheric Sciences*,
 804 *29*(1), 11–37.
- 805 Hoskins, B. J., Draghici, I., & Davies, H. (1978). A new look at the ω -equation.
 806 *Quarterly Journal of the Royal Meteorological Society*, *104*(439), 31–38.
- 807 Hoskins, B. J., & James, I. N. (2014). *Fluid dynamics of the mid-latitude atmo-*
 808 *sphere*. John Wiley & Sons.
- 809 Jin, X., Najjar, R., Louanchi, F., & Doney, S. C. (2007). A modeling study of the
 810 seasonal oxygen budget of the global ocean. *Journal of Geophysical Research:*
 811 *Oceans*, *112*(C5).
- 812 Johnston, T. S., MacKinnon, J. A., Colin, P. L., Haley, P. J., Lermusiaux, P. F., Lu-
 813 cas, A. J., ... others (2019). Energy and momentum lost to wake eddies and
 814 lee waves generated by the north equatorial current and tidal flows at peleliu,
 815 palau. *Oceanography*, *32*(4), 110–125.
- 816 Klymak, J. M., Shearman, R. K., Gula, J., Lee, C. M., D’Asaro, E. A., Thomas,
 817 L. N., ... others (2016). Submesoscale streamers exchange water on the north
 818 wall of the gulf stream. *Geophysical Research Letters*, *43*(3), 1226–1233.
- 819 Lévy, M., Bopp, L., Karleskind, P., Resplandy, L., Éthé, C., & Pinsard, F. (2013).
 820 Physical pathways for carbon transfers between the surface mixed layer and
 821 the ocean interior. *Global Biogeochemical Cycles*, *27*(4), 1001–1012.
- 822 Llanillo, P., Pelegrí, J. L., Talley, L., Peña-Izquierdo, J., & Cordero, R. (2018). Oxy-
 823 gen pathways and budget for the eastern south pacific oxygen minimum zone.
 824 *Journal of Geophysical Research: Oceans*, *123*(3), 1722–1744.
- 825 MacGilchrist, G. A., Marshall, D. P., Johnson, H. L., Lique, C., & Thomas, M.
 826 (2017). Characterizing the chaotic nature of ocean ventilation. *Journal of*
 827 *Geophysical Research: Oceans*, *122*(9), 7577–7594.
- 828 Mahadevan, A., D’Asaro, E. A., Allen, J. T., Almaraz García, P., Alou-Font, E.,
 829 Aravind, H. M., ... Zarokanellos, N. (2020). *Calypso 2019 cruise report: field*
 830 *campaign in the mediterranean* (Tech. Rep.). WHOI Tech. Rep. WHOI-2020-
 831 01, <https://hdl.handle.net/1912/25266>. doi: 10.1575/1912/25266
- 832 Mahadevan, A., D’asaro, E., Lee, C., & Perry, M. J. (2012). Eddy-driven stratifica-
 833 tion initiates north atlantic spring phytoplankton blooms. *Science*, *337*(6090),
 834 54–58.
- 835 Mahadevan, A., Oliger, J., & Street, R. (1996a). A nonhydrostatic mesoscale ocean
 836 model. Part II: Numerical implementation. *Journal of Physical Oceanography*,
 837 *26*(9), 1881–1900.
- 838 Mahadevan, A., Oliger, J., & Street, R. (1996b). A nonhydrostatic mesoscale ocean
 839 model. Part I: Well-posedness and scaling. *Journal of Physical Oceanography*,

- 840 26(9), 1868-1880.
- 841 Mahadevan, A., & Tandon, A. (2006). An analysis of mechanisms for submesoscale
842 vertical motion at ocean fronts. *Ocean Modelling*, 14(3-4), 241–256.
- 843 Mahadevan, A., Tandon, A., & Ferrari, R. (2010). Rapid changes in mixed layer
844 stratification driven by submesoscale instabilities and winds. *Journal of Geo-*
845 *physical Research: Oceans*, 115(C3).
- 846 McWilliams, J. C. (2016). Submesoscale currents in the ocean. *Proceedings of the*
847 *Royal Society A: Mathematical, Physical and Engineering Sciences*, 472(2189),
848 20160117.
- 849 McWilliams, J. C., Gula, J., & Molemaker, M. J. (2019). The gulf stream north
850 wall: Ageostrophic circulation and frontogenesis. *Journal of Physical Oceanog-*
851 *raphy*, 49(4), 893–916.
- 852 McWilliams, J. C., Gula, J., Molemaker, M. J., Renault, L., & Shchepetkin, A. F.
853 (2015). Filament frontogenesis by boundary layer turbulence. *Journal of*
854 *Physical Oceanography*, 45(8), 1988–2005.
- 855 Munk, W., Armi, L., Fischer, K., & Zachariasen, F. (2000). Spirals on the sea. *Pro-*
856 *ceedings of the Royal Society of London. Series A: Mathematical, Physical and*
857 *Engineering Sciences*, 456(1997), 1217–1280.
- 858 Nurser, A. G., & Marshall, J. C. (1991). On the relationship between subduction
859 rates and diabatic forcing of the mixed layer. *Journal of physical oceanography*,
860 21(12), 1793–1802.
- 861 Omand, M. M., D’Asaro, E. A., Lee, C. M., Perry, M. J., Briggs, N., Cetinić, I., &
862 Mahadevan, A. (2015). Eddy-driven subduction exports particulate organic
863 carbon from the spring bloom. *Science*, 348(6231), 222–225.
- 864 Palevsky, H. I., & Nicholson, D. P. (2018). The north atlantic biological pump: in-
865 sights from the ocean observatories initiative irvinger sea array. *Oceanography*,
866 31(1), 42–49.
- 867 Pascual, A., Ruiz, S., Olita, A., Troupin, C., Claret, M., Casas, B., . . . others
868 (2017). A multiplatform experiment to unravel meso-and submesoscale pro-
869 cesses in an intense front (alborex). *Frontiers in Marine Science*, 4, 39.
- 870 Pollard, R. T., & Regier, L. A. (1992). Vorticity and vertical circulation at an ocean
871 front. *Journal of Physical Oceanography*, 22(6), 609-625.
- 872 PSOM. (2020, 6). Retrieved from <https://doi.org/10.5281/zenodo.3902273>
- 873 Ramachandran, S., Tandon, A., & Mahadevan, A. (2014). Enhancement in verti-
874 cal fluxes at a front by mesoscale-submesoscale coupling. *Journal of Geophysi-*
875 *cal Research: Oceans*, 119(12), 8495–8511.

- Resplandy, L., Lévy, M., & McGillicuddy Jr, D. J. (2019). Effects of eddy-driven subduction on ocean biological carbon pump. *Global Biogeochemical Cycles*, *33*(8), 1071–1084.
- Rocha, C. B. (2015, 9). *pyspec*. Retrieved from <https://doi.org/10.5281/zenodo.31596>
- Rotunno, R., Skamarock, W. C., & Snyder, C. (1994). An analysis of frontogenesis in numerical simulations of baroclinic waves. *Journal of the atmospheric sciences*, *51*(23), 3373–3398.
- Ruiz, S., Claret, M., Pascual, A., Olita, A., Troupin, C., Capet, A., ... others (2019). Effects of oceanic mesoscale and submesoscale frontal processes on the vertical transport of phytoplankton. *Journal of Geophysical Research: Oceans*, *124*(8), 5999–6014.
- Samelson, R. (1992). Fluid exchange across a meandering jet. *Journal of physical oceanography*, *22*(4), 431–444.
- Shcherbina, A. Y., & D’Asaro, E. A. (2020). Direct observations of submesoscale modulation of ocean surface boundary layer turbulence. In *Ocean sciences meeting 2020*.
- Shcherbina, A. Y., Sundermeyer, M. A., Kunze, E., D’Asaro, E., Badin, G., Birch, D., ... others (2015). The latmix summer campaign: submesoscale stirring in the upper ocean. *Bulletin of the American Meteorological Society*, *96*(8), 1257–1279.
- Siegelman, L. (2020). Energetic submesoscale dynamics in the ocean interior. *Journal of Physical Oceanography*, *50*(3), 727–749.
- Siegelman, L., Klein, P., Rivière, P., Thompson, A. F., Torres, H. S., Flexas, M., & Menemenlis, D. (2020). Enhanced upward heat transport at deep submesoscale ocean fronts. *Nature Geoscience*, *13*(1), 50–55.
- Skyllingstad, E. D., Duncombe, J., & Samelson, R. M. (2017). Baroclinic frontal instabilities and turbulent mixing in the surface boundary layer. part ii: Forced simulations. *Journal of Physical Oceanography*, *47*(10), 2429–2454.
- Smith, K. M., Hamlington, P. E., & Fox-Kemper, B. (2016). Effects of submesoscale turbulence on ocean tracers. *Journal of Geophysical Research: Oceans*, *121*(1), 908–933.
- Spall, M. A. (1995). Frontogenesis, subduction, and cross-front exchange at upper ocean fronts. *Journal of Geophysical Research: Oceans*, *100*(C2), 2543–2557.
- Spiro Jaeger, G. V. R. (2019). *Stratified and stirred: monsoon freshwater in the bay of bengal* (Unpublished doctoral dissertation). Massachusetts Institute of Technology.

- 913 Stamper, M. A., Taylor, J. R., & Fox-Kemper, B. (2018). The growth and satura-
 914 tion of submesoscale instabilities in the presence of a barotropic jet. *Journal of*
 915 *Physical Oceanography*, 48(11), 2779–2797.
- 916 Stanley, R. H., McGillicuddy Jr, D. J., Sandwith, Z. O., & Pleskow, H. M. (2017).
 917 Submesoscale hotspots of productivity and respiration: Insights from high-
 918 resolution oxygen and fluorescence sections. *Deep Sea Research Part I:*
 919 *Oceanographic Research Papers*, 130, 1–11.
- 920 Stommel, H. (1979). Determination of water mass properties of water pumped
 921 down from the ekman layer to the geostrophic flow below. *Proceedings of the*
 922 *National Academy of Sciences*, 76(7), 3051–3055.
- 923 Taylor, J. R., Bachman, S., Stamper, M., Hosegood, P., Adams, K., Sallee, J.-B., &
 924 Torres, R. (2018). Submesoscale rossby waves on the antarctic circumpolar
 925 current. *Science advances*, 4(3), eaao2824.
- 926 Taylor, J. R., Smith, K. M., & Vreugdenhil, C. A. (2020). The influence of sub-
 927 mesoscales and vertical mixing on the export of sinking tracers in large-eddy
 928 simulations. *Journal of Physical Oceanography*(2020).
- 929 Thomas, L. N. (2008). Formation of intrathermocline eddies at ocean fronts by
 930 wind-driven destruction of potential vorticity. *Dynamics of atmospheres and*
 931 *oceans*, 45(3-4), 252–273.
- 932 Thomas, L. N., & Joyce, T. M. (2010). Subduction on the northern and southern
 933 flanks of the gulf stream. *Journal of physical oceanography*, 40(2), 429–438.
- 934 Thomas, L. N., Tandon, A., & Mahadevan, A. (2008). Submesoscale processes and
 935 dynamics. *Ocean modeling in an Eddying Regime*, 177, 17-38.
- 936 Thomas, L. N., Taylor, J. R., Ferrari, R., & Joyce, T. M. (2013). Symmetric in-
 937 stability in the gulf stream. *Deep Sea Research Part II: Topical Studies in*
 938 *Oceanography*, 91, 96–110.
- 939 Verma, V., Pham, H. T., & Sarkar, S. (2019). The submesoscale, the finescale and
 940 their interaction at a mixed layer front. *Ocean Modelling*, 140, 101400.
- 941 Vries, P., & Döös, K. (2001). Calculating lagrangian trajectories using time-
 942 dependent velocity fields. *Journal of Atmospheric and Oceanic Technology*,
 943 18(6), 1092–1101.
- 944 Wang, D.-P. (1993). Model of frontogenesis: Subduction and upwelling. *Journal of*
 945 *Marine Research*, 51(3), 497–513.
- 946 Wenegrat, J. O., Thomas, L. N., Gula, J., & McWilliams, J. C. (2018). Effects
 947 of the submesoscale on the potential vorticity budget of ocean mode waters.
 948 *Journal of Physical Oceanography*, 48(9), 2141–2165.

- 949 Yin, W., & Huang, D. (2016). Evolution of submesoscale coastal frontal waves in the
 950 east china sea based on geostationary ocean color imager observational data.
 951 *Geophysical Research Letters*, 43(18), 9801–9809.
- 952 Yu, X., Naveira Garabato, A. C., Martin, A. P., Buckingham, C. E., Brannigan,
 953 L., & Su, Z. (2019). An annual cycle of submesoscale vertical flow and re-
 954 stratification in the upper ocean. *Journal of Physical Oceanography*, 49(6),
 955 1439–1461.